Published in IET Biometrics
Received on 26th April 2013
Revised on 22nd July 2013
Accepted on 22nd August 2013
doi: 10.1049/iet-bmt.2013.0039

ISSN 2047-4938

Periocular biometrics: constraining the elastic graph matching algorithm to biologically plausible distortions

Hugo Proença, Juan C. Briceño

Department of Computer Science, IT – Instituto de Telecomunicações, University of Beira Interior, 6200-Covilhã, Portugal
E-mail: hugomcp@di.ubi.pt

Abstract: In biometrics research, the periocular region has been regarded as an interesting trade-off between the face and the iris, particularly in unconstrained data acquisition setups. As in other biometric traits, the current challenge is the development of more robust recognition algorithms. Having investigated the suitability of the 'elastic graph matching' (EGM) algorithm to handle non-linear distortions in the periocular region because of facial expressions, the authors observed that vertices locations often not correspond to displacements in the biological tissue. Hence, they propose a 'globally coherent' variant of EGM (GC-EGM) that avoids sudden local angular movements of vertices while maintains the ability to faithfully model non-linear distortions. Two main adaptations were carried out: (i) a new term for measuring vertices similarity and (ii) a new term in the edges-cost function penalises changes in orientation between the model and test graphs. Experiments were carried out both in synthetic and real data and point for the advantages of the proposed algorithm. Also, the recognition performance when using the EGM and GC-EGM was compared, and statistically significant improvements in the error rates were observed when using the GC-EGM variant.

.

1 Introduction

Biometric recognition systems are known to provide outstanding levels of performance and constitute a particularly successful case in the pattern recognition area [1]. Owing to this, current efforts are mainly concentrated in the development of algorithms to increase the robustness to uncontrolled data acquisition environments. Here, the periocular region emerged as an interesting trait: it contains the eye and its immediate vicinity (eyelids, eyelashes, nearby skin area and eyebrows) and is a trade-off between the whole face and the iris alone; it is easy to acquire without user cooperation and does not require a controlled lighting setup. Examples of relevant works on periocular recognition are because of Park *et al.* [2] and Woodard *et al.* [3].

Proposed by Lades *et al.* [4], the 'elastic graph matching' (EGM) algorithm is a popular choice for handling non-linear local distortions. Its insight is the concept of 'dynamic link architecture', that models the structure of the brain in terms of graphs. Most of the works in this scope regarding the face recognition problem, but other applications are reported in the literature: Cao *et al.* [5], for recognising facial expressions; Zhao *et al.* [6], for face alignment; and Stamou *et al.* [7], for object tracking. The EGM receives a pair of images to match: the 'model' and the 'test'. Two graphs are superimposed on these and local deformation parameters are estimated: at first, a global phase finds the initial position and scaling factor for the test graph; then, the local deformation parameters are sought iteratively by a simulated annealing-based strategy.

1.1 Motivation and problem description

There is no other part of the human body where as many muscles interact as in the face. Regarding the periocular region, muscles from the 'orbicularis oculi' family play a major role, but also muscles of the 'nasalis, procerus, quadratus labii superioris' and 'levator labii superioris' families determine the non-linear distortions because of expressions [8]. As an illustration, Fig. 1 gives two samples of a subject with neutral (top-left) and happy (top-right) expressions. The bottom image illustrates the changes in appearance, where brightness directly corresponds to the magnitude of changes.

Owing to the bio-mechanical nature of movements, some cases are particularly improbable: (i) sudden local angular distortions rarely occur, that is, the angles between adjacent regions tend to be preserved. (ii) There is a strong spatial correlation of displacements, determined by skin elasticity. Having investigated the suitability of the EGM algorithm to handle the effect of facial expressions, two major weaknesses were observed: the algorithm allows changes in the position of vertices that are practically impossible because of biological constraints. Also, the magnitude of

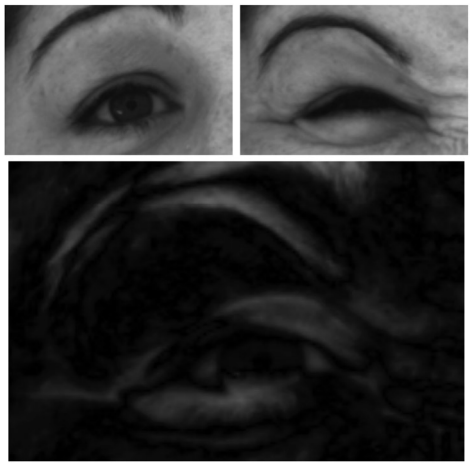

Fig. 1 *Changes inside the periocular region because of facial expressions*

Top-left image regards a neutral expression and the top-right image has a 'happy' expression. Image at the bottom shows the magnitude of the differences between the aligned images, where brightness corresponds to most notorious changes

the displacements with respect to neighbour vertices is often less correlated than it should.

Accordingly, this paper proposes two changes to the EGM algorithm, and optimises its performance for periocular recognition purposes. Changes regarding the matching cost function, aiming at: (i) avoid sudden changes in the angular location of vertices and (ii) handle slight changes in scale/rotation in a better way, which often decrease the correlation of displacements of neighbour vertices.

As illustrated in Fig. 2, angular distortions in the EGM test graphs are frequent when the edges cost $\mathcal{S}_e$ is small (Fig. 2*b*). In this case, the location of most vertices in the test data is accurately determined, but a few relevant exceptions occur (highlighted by the dashed circles). This problem is not alleviated if the edges cost is increased, as the algorithm weakens its modelling ability (continuous ellipse in Fig. 2*d*). The variant of the EGM algorithm introduced in this paper (Fig. 2*c*), henceforth designated as 'globally coherent EGM' (CG-EGM), faithfully addresses the typical distortions in the periocular region. Also, it should be stressed that improvements in performance were obtained without significant increases in the computational burden of the matching process.

1.2 Related work

Several works about the EGM algorithm are reported in the literature: Tefas *et al.* [9] reformulated the Fisher's discriminant ratio to a quadratic optimisation problem subject to a set of inequality constraints, finding the optimal separating hyperplanes and the polynomial decision surfaces. Shin *et al.* [10] augmented the robustness of Gabor jets information to changes in scale and rotation by Fourier analysis. A new edges cost term forces that the difference in angle of the corresponding edges in the model and test graphs is below a threshold. Zafeiriou *et al.* [11] used eigen-analysis to find the most discriminant features from the jets and proposed a new similarity measure for these. This work was subsequently extended in [12], by proposing a similarity measure that fuses the feature distance to nodes deformation. Also, the local similarity values in the graph were weighted by coefficients derived from discriminant analysis. More recently, Zafeiriou and Pitas [13] proposed a technique for the selection of the most discriminant facial landmarks for recognising facial expressions. A kernel-based technique for feature extraction is presented, concluding about significant improvements in performance, when compared with the Gabor-based and morphological variants of EGM.

Variations in the pre-processing phase of EGM aim at data normalisation, in order to make easier the subsequent processing phases. Kela *et al.* [14] used the Retinex colour constancy algorithm before the feature extraction process. Shin *et al.* [15] proposed an extension to faithfully handle globally warped faces, by introducing warping-compensated edges in the graph matching cost function. The method is based in a feature set more robust to changes in scale and rotation than Gabor coefficients. Also, a modified cost function compensates for global affine warps between faces. Kotropoulos *et al.* [16] introduced the concept of morphological elastic graph matching, which main discriminating point is the use of multi-scale morphological operations to replace the Gabor-based image representation phase. They proposed a probabilistic hill climbing algorithm that does not distinguish between coarse and fine matching. Finally, Serradell *et al.* [17] proposed a

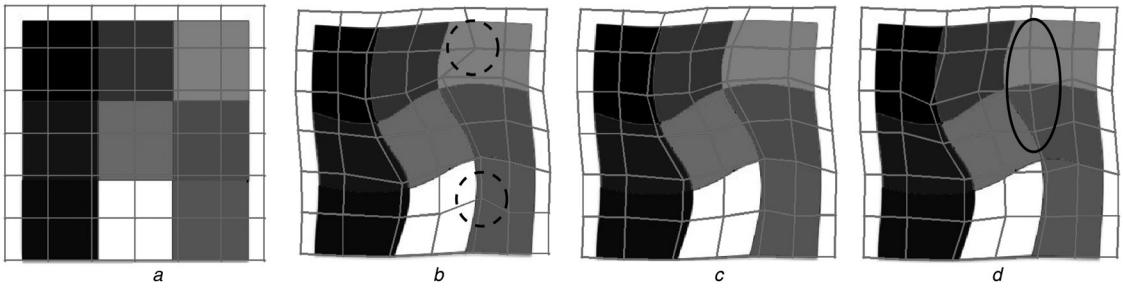

Fig. 2 *Illustration of a sudden angular deformation (denoted by the dashed circles in Fig. 2b), frequent in the EGM algorithm*

These are movements of isolated vertices unlikely in biological data. At the other extreme, if the edges cost is too high, the algorithm weakens its modelling ability (solid ellipse in Fig. 2*d*)
Small $\mathcal{S}_e$ cost
a Model graph
b EGM
Large $\mathcal{S}_e$ cost
c GC-EGM
d EGM

doi: 10.1049/iet-bmt.2013.0039

geometric graph matching schema based on edges shape, finding an affine transform that maps the test and the model data. Non-linear deformations were modelled as Gaussian processes and sets of neighbour edges grouped into 'super-edges' used in matching.

Based in the analysis of the above-described works, it is evident that no previous work has focused on the specificities of movements inside the periocular region, which are far more constrained than in the case of the face. This is the main motivation for the work described in this paper: to propose a variant of the EGM particularly suitable to model the distortions inside the periocular region.

As above summarised, none of the previously published variants of the EGM adapts the behaviour of the algorithm to the types of movements that are biologically possible for a specific region. Hence, the variant proposed in this paper can be regarded as an attempt to model biologically plausible movements, by (i) adding a new term to the edges-cost function and (ii) improving the robustness of the terms that measures the similarity between jets. Our motivations (and experiments) were focused in the periocular recognition problem, but a similar approach might be used for other types of biometric traits, according to its plausible deformations. This is also regarded as a strong point of the method proposed in this paper.

The remainder of this paper is organised as follows: Section 2 summarises the EGM algorithm. Section 3 provides a description of the proposed changes. Section 4 presents and discusses the results and the conclusions are given in Section 5.

2 Elastic graph matching algorithm

Let I be a greyscale image. The process starts by convolving I with a set of Gabor kernels $\psi_{\boldsymbol{k}}$ [18], where $\boldsymbol{k}$ denotes the wavelength and orientation of the kernel. The operator $\mathcal{W}$ symbolises the convolution of I with all possible parameterisations for $\boldsymbol{k}$

$$(\mathcal{W}I)(\boldsymbol{k}) = \psi_{\boldsymbol{k}} \times I \tag{1}$$

A local description of I is obtained by sampling $\mathcal{W}$ at logarithmically spaced frequency levels υ and linearly spaced orientations μ

$$\boldsymbol{k}_{\upsilon,\mu} = k_{\upsilon} e^{i\phi_{\mu}} \tag{2}$$

being $k_{\upsilon} = k_m / f^{\upsilon}$, $\phi_{\mu} = \pi\mu/n$, n is the number of orientations and f is the spacing factor between kernels in the frequency domain. The coefficients of $(\mathcal{W}I)\boldsymbol{k}_{\upsilon,\mu}$ constitute a feature vector that describes the local properties of each image point $\boldsymbol{x}$, and is called a 'jet' $\mathcal{J}$. Hence, a jet is a set of complex coefficients for each image point, that is, $\mathcal{J} = \{\mathcal{J}_j\} = \{a_j e^{i\phi_j}\}$. A similarity function between jets is given by

$$\mathcal{S}_1(\mathcal{J}^M, \mathcal{J}^T) := \frac{\sum_j a_j a'_j}{\sqrt{\sum_j a_j^2 \sum_j a_j'^2}} \tag{3}$$

being $\mathcal{J}^M$ and $\mathcal{J}^T$ the jets extracted from the model and test images. Considering that phase is ignored in $\mathcal{S}_1$, this function behaves poorly against slight changes in translation, which gave insight to a variant that considers both magnitude and phase coefficients [19]

$$\mathcal{S}_2(\mathcal{J}^M, \mathcal{J}^T) := \frac{\sum_j a_j a'_j \cos\left(\phi_j - \phi'_j\right)}{\sqrt{\sum_j a_j^2 \sum_j a_j'^2}} \tag{4}$$

Edges encode information about the relative position of vertices and enforce topology preservation. During the matching process, this is imposed by penalising changes in the length of edges between corresponding vertices in the model and test graphs

$$\mathcal{S}_{e_1}\left(\boldsymbol{\Delta}^M_{i,j}, \boldsymbol{\Delta}^T_{i,j}\right) := \frac{\left(\boldsymbol{\Delta}^M_{i,j} - \boldsymbol{\Delta}^T_{i,j}\right)^2}{\left(\boldsymbol{\Delta}^M_{i,j}\right)^2} \tag{5}$$

being $\Delta_{i,j}$ the length of the edge between the ith and jth vertices. According to the above, the similarity between graphs is given by

$$\mathcal{C}(\boldsymbol{x}^T) := \lambda \sum_{i,j \in E} \mathcal{S}_e\left(\boldsymbol{\Delta}^M_{i,j}, \boldsymbol{\Delta}^T_{i,j}\right) - \sum_{i \in V} \mathcal{S}_{1,2}(\mathcal{J}^T(\boldsymbol{x}^T), \mathcal{J}^M) \tag{6}$$

Finally, the algorithm seeks iteratively for the position of vertices in the test graph that minimises $\mathcal{C}(\boldsymbol{x}^T)$.

3 Globally coherent elastic graph matching

Let $\mathcal{J}^{\upsilon} = \{\mathcal{J}^{\upsilon}_1, \ldots, \mathcal{J}^{\upsilon}_k\}$ be an arrangement of $\mathcal{J}$, such that elements in the jet are sorted according to the magnitude υ of the Gabor kernels. Also, $\mathcal{J}^{\mu}$ is an arrangement with items sorted according to the orientation of the Gabor kernels. The similarity between jets in the model $\mathcal{J}^M$ and test $\mathcal{J}^T$ graphs is given by the maximum value of the derivative with respect to time of the sample cross-correlation

$$\mathcal{S}_3(\mathcal{J}^M, \mathcal{J}^T) := \max\left\{\max\left(\frac{\partial}{\partial t}\left|a^M_* \bigstar a^T_*\right|\right), \max\left(\frac{\partial}{\partial t}\left|\phi^M_* \bigstar \phi^T_*\right|\right)\right\} \tag{7}$$

being $\bigstar$ the cross-correlation operator, t denotes time (vector position), a_* and ϕ_* are the normalised version of coefficients of $\mathcal{J}^{\upsilon}$ and $\mathcal{J}^{\mu}$, so that autocorrelations at zero lag yield 1.0 value. As illustrated in Fig. 3, $\mathcal{S}_3$ finds the similarity peak of $\mathcal{J}^M$ and $\mathcal{J}^T$ with different time-lags applied to one of them. Intuitively, in case of a change in scale between corresponding regions, correlation attains a maximum when $\mathcal{J}^T$ is shifted by the corresponding amount. Fig. 3*b* illustrates three derivatives of the cross-correlation values: for extremely correlated jet coefficients without time-lag (dark grey line), for moderately correlated signals with slight time-lag (light grey line) and poorly correlated signals (grey line).

Also, a term was added to the edges-cost function, relating the orientation of corresponding edges in the model and test graphs. This term is in the $]-1, 1[$ interval and penalises changes in orientation, constituting a topology reinforcement factor. Let $v_1 = (x_1, y_1)$ and $v_2 = (x_2, y_2)$ be adjacent vertices and $\boldsymbol{v} = (x_1, y_1) - (x_2, y_2)$ a vector connecting these points. The new edges-cost function is

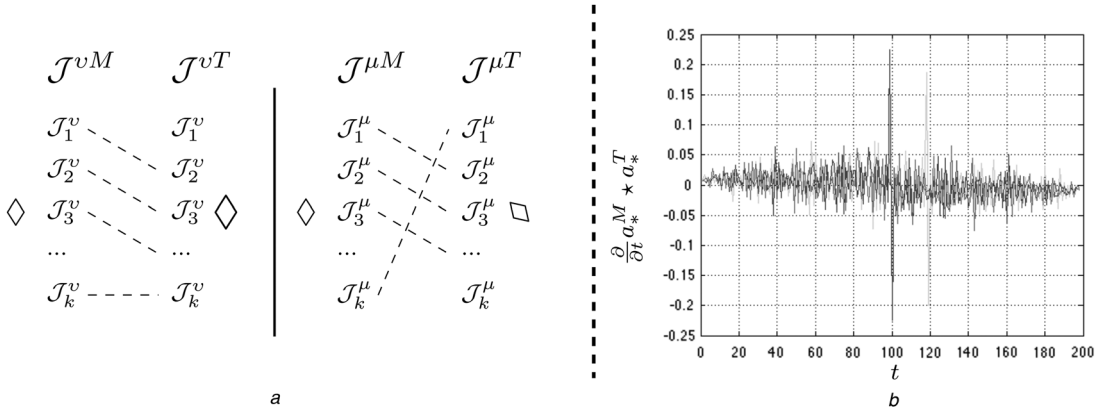

Fig. 3 *Rationale behind the proposed function to measure jets similarity. In image*

a Change in scale leads to maximal cross-correlation when a time-lag is applied to one of the jet coefficients of $\mathcal{J}^v$. A change in rotation leads to a similar phenomenon, using $\mathcal{J}^\mu$. The dashed lines denote the corresponding jet coefficients that maximally correlate

b Derivatives of the cross-correlation with respect to time are given: highly correlated (dark grey line), moderately correlated (light grey line) and poorly correlated (grey line) jet coefficients are shown

given by

$$\mathcal{S}_{e_2}\left(\mathbf{\Delta}_{i,j}^M,\ \mathbf{\Delta}_{i,j}^T\right) := \frac{\left(\mathbf{\Delta}_{i,j}^M - \mathbf{\Delta}_{i,j}^T\right)^2 \lambda_\theta\left((1+\delta) - \left(\left(\boldsymbol{v}^M\,\boldsymbol{v}^T\right)/\left(\|\boldsymbol{v}^M\|\,\|\boldsymbol{v}^T\|\right)\right)\right)}{\left(\mathbf{\Delta}_{i,j}^M\right)^2} \tag{8}$$

being λ_θ a parameter that controls the amount of angular distortions allowed, $\boldsymbol{v}^M$ and $\boldsymbol{v}^T$ the vectors in the model and test graphs and δ a small positive constant. Fig. 4 illustrates the rationale behind the proposed edges-cost function. The grey line segment represents an edge in the model graph. The grey surfaces compare the values of $\mathcal{S}_{e_1}$ (upper figure) and the proposed variant $\mathcal{S}_{e_2}$ (bottom figure), with respect to the location of vertex v_2 in the test graph (axes x and y), keeping the same location for v_1. The insight is to consider both the edge length and orientation, increasing the cost when these values differ from the model graph.

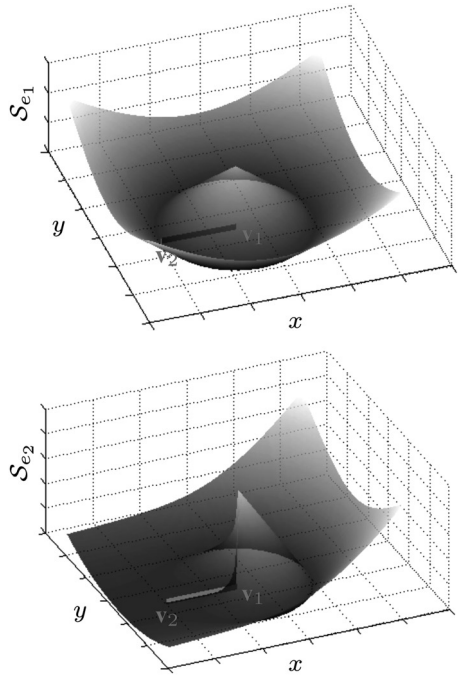

Fig. 4 *Comparison between the edges cost in the EGM algorithm (upper figure) and in the GC-EGM variant (bottom figure)*

Orientation of the edge in the model graph is denoted by the grey line and the axes x and y correspond to the position of the v_2 vertex in the test graph, while maintaining the location of v_1

4 Experiments and discussion

Initially, the comparison of performance between the EGM algorithm and the proposed variant (GC-EGM) was carried out in synthetic data, highlighting the behaviour of both algorithms. Next, experiments were focused on the periocular region, being divided into two parts: (i) comparing the errors in keypoints registration and (ii) comparing the recognition performance, which at the bottom level is the meaningful factor. The optimisation of the EGM and GC-EGM was done by exhaustive parameter evaluation in a completely disjoint training data set, selecting the parameters that minimise the registration or recognition error rates.

4.1 Synthetic deformations

Four images with evident textures [http://www.freestocktextures.com/texture/] – graffitis, wood, wall and soil – were used and warped by a radial basis function. Both algorithms were tested in this data and the errors in keypoint registration obtained

$$E = \frac{1}{t\,w\,h}\sum_{j=1}^{t}\left\|\left(x_j^{(\mathrm{T})},\ y_j^{(\mathrm{T})}\right) - \left(x_j^{(\mathrm{G})},\ y_j^{(\mathrm{G})}\right)\right\|_2 \tag{9}$$

being (w, h) the image dimensions, $(x_j^{(\mathrm{T})}, y_j^{(\mathrm{T})})$ the location of the jth vertex in the test graph, $(x_j^{(\mathrm{G})}, y_j^{(\mathrm{G})})$ the ground-truth location and t the number of vertices in the graph.

Results are given in Fig. 5, showing the error (9) below each image. E_o denotes the error of the EGM and E_p gives the error of the GC-EGM variant. In each image, the dark grey lines represent the test graphs of the EGM and the

doi: 10.1049/iet-bmt.2013.0039

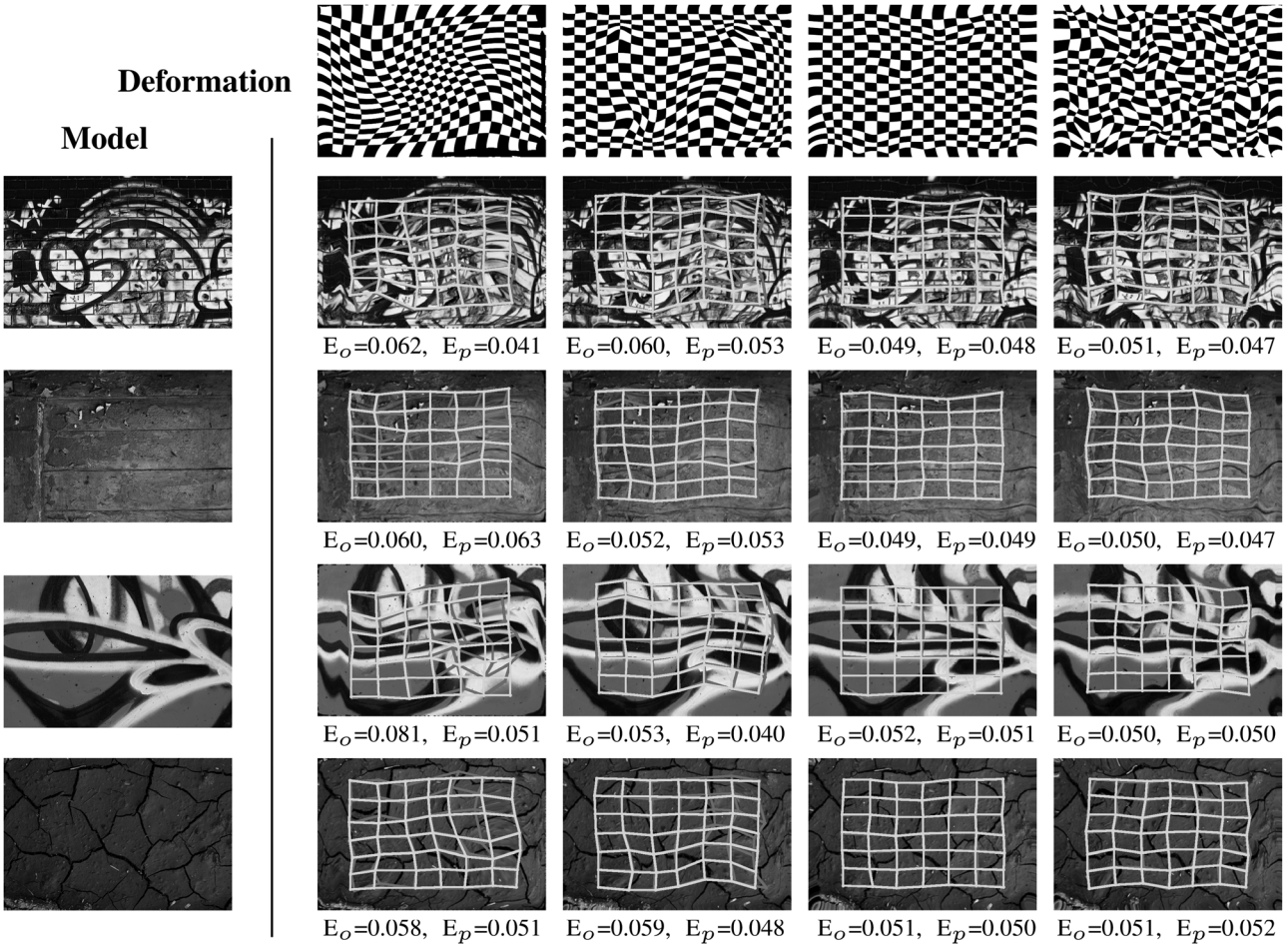

Fig. 5 *Comparison between the error rates (9) obtained by the EGM algorithm (dark grey lines, errors denoted by E_o) and the proposed GC-EGM variant (light grey lines, errors denoted by E_p)*

light grey lines of the GC-EGM. It should be stressed that error rates correspond to the median values observed, when repeating the coarse (global) to fine (local) optimisation processes twenty times per image/deformation.

Using the EGM as baseline, improvements were observed in about 80% of the times, with an average decrease of the error (9) near 8.40% (0.056 for the EGM and 0.051 for the GC-EGM). Also, improvements were consistent among images tested and for all the deformations. The slight differences in performance among images – for a given deformation – were explained by the different amounts of information extracted by the Gabor jets configuration, that obviously are data-dependent (four logarithmic spaced wavelengths and four rotation angles linearly spaced were used).

4.2 Periocular region: keypoints registration

Subsequently, a set of 100 images from the 'FaceExpressUBI' data set [http://www.di.ubi.pt/~hugomcp/EEGM] was used to compare the errors in keypoint registration between the EGM and GC-EGM algorithms. For each image, thirteen keypoints were manually marked in the model and test images, corresponding to prominent landmarks in the periocular region: eye corners (two keypoints), iris centre (one), eyelids (four) and eyelashes (six). Two versions of the experiment were carried out: (i) using dense grids of t vertices, t:$7 \times 7 = 49$ and t:$14 \times 14 = 196$ to initialise the model and test graphs and (ii) using sparse grids, comprising exclusively the manually annotated landmarks. As in the experiments described in Section 4.1, performance corresponds to the median error between vertices in the test graph and the ground-truth.

Results are illustrated in Fig. 6 and summarised in Table 1. Various parameters for the Gabor kernels were used, assessing the impact on performance. Overall, the GC-EGM was consistently better with non-overlapping confidence intervals, yielding decreases in the error rates of about 15% for dense grids and 25% for sparse grids. The dimension of the feature space used in the jets only slightly improved the results, whereas the effect of the number of vertices used was much more evident. As expected, GC-EGM avoids sudden changes in the location of vertices, and reinforces topology preservation. The former observation was particularly evident for graphs of sparse vertices, because of the smaller number of edges. Also, the error rates observed for sparse graphs were consistently higher than for dense graphs, which we believe to have similar justification (smaller number of edges).

4.3 Periocular region: recognition performance

In the final – and most important – experiment, we assessed whether the GC-EGM contributes for improvements in recognition performance, when compared with the EGM. Here, the state-of-the-art periocular recognition algorithm (because of Park *et al.* [2]) was used. The best configurations observed for the EGM and GC-EGM in the

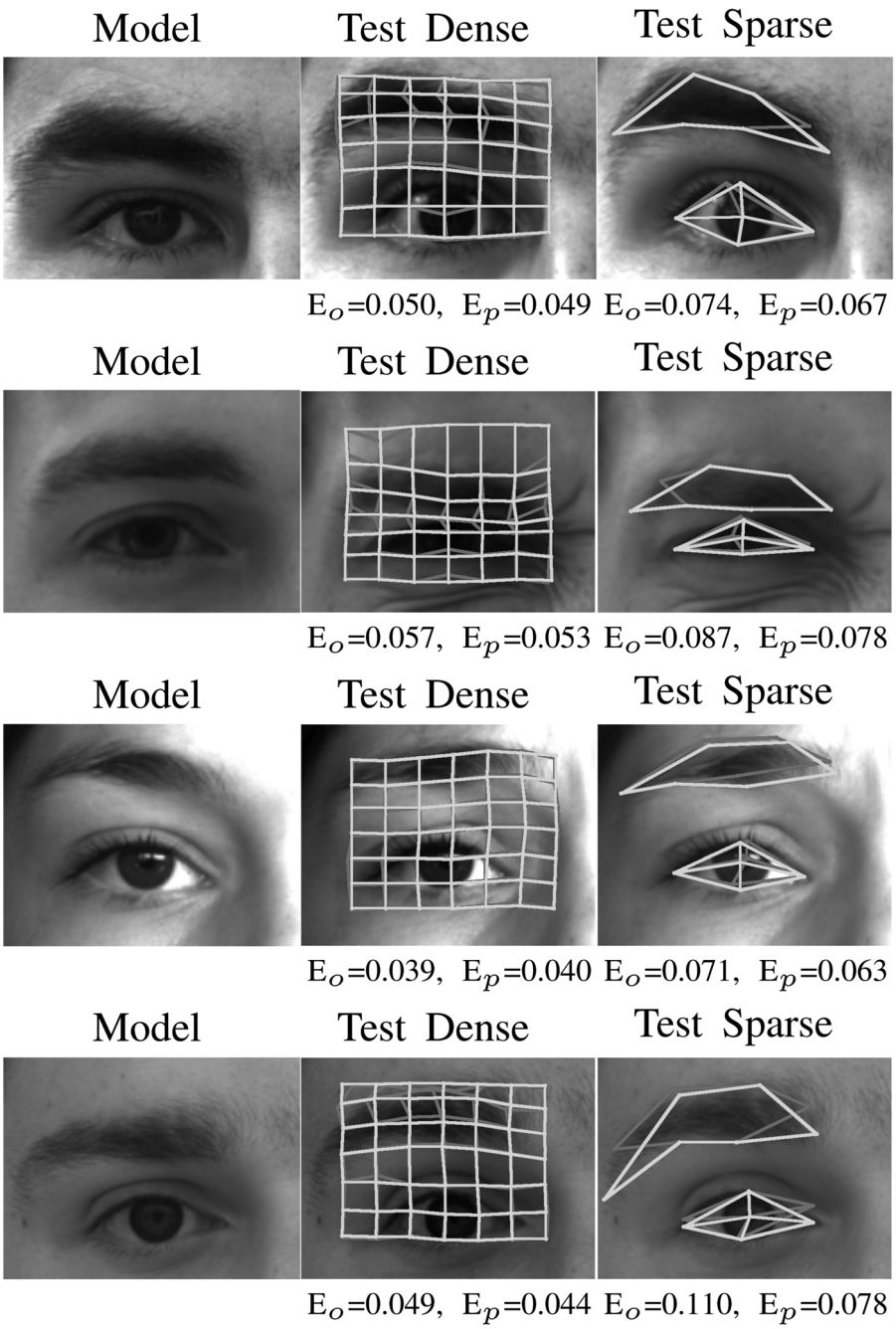

Fig. 6 *Examples of the results obtained by the EGM algorithm (dark grey lines) and the proposed GC-EGM variant (light grey lines) in modelling the distortions in the periocular region because of facial expressions*

experiments of Section 4.2 were used: 14×14 dense grids (196 vertices), each one described by 48 Gabor kernels. Of about 2000 images of the 'FaceExpressUBI' data set from 100 subjects (20 frames per subject) were used, giving a total of 8550 genuine and 950 000 impostor comparisons (only comparisons between images of different sessions were considered, guaranteeing the independence between image pairs). Local binary patterns (LBPs) [20] and histograms of oriented gradients [21] (HOGs) provided a global description of the periocular region, extracted from rectangular patches defined by adjacent graph vertices. Plus, the scale invariant feature transform [22] (SIFT) was used as local feature descriptor. For every pair of images, HOGs and LBPs were concatenated and matched by the Chi-square distance. The number of keypoints correspondences was used as matching score for the SIFT. Subsequently, results were fused at the score level, by a weighted linear scheme. Having a set of scores s_i, the final response of the system was given by

$$\hat{s} = \sum_{i=1}^{N} w_i s_i \tag{10}$$

where w_i is the weight assigned to output of ith classifier (weights were optimised by a logistic regression procedure [23]), and N is the number of scores to be fused ($N = 3$).

Park *et al.* [2] used as reference point of the centre of the iris with radius r, and defined the periocular region-of-interest (ROI) as a $3r \times 4r$ rectangle centred at the iris. This is only satisfactory in case of frontal gazes. As the iris is a moving component, in case of deviated gaze,

doi: 10.1049/iet-bmt.2013.0039

Table 1 Summary of the error rates (9) observed by the original EGM algorithm and the proposed variant GC-EGM in modelling the effect of facial expressions in periocular images

Algorithm	Error	95% Conf. Int.l	Parameters
EGM	0.051	±0.002	7 × 7 dense grid; Gabor jet: four wavelengths and four orientations
GC-EGM	0.043	±0.001	7 × 7 dense grid; Gabor jet: four wavelengths and four orientations
EGM	0.031	±0.001	14 × 14 dense grid; Gabor jet: four wavelengths and four orientations
GC-EGM	0.026	±0.001	14 × 14 dense grid; Gabor jet: four wavelengths and four orientations
EGM	0.049	±0.002	7 × 7 dense grid; Gabor jet: eight wavelengths and six orientations
GC-EGM	0.042	±0.001	7 × 7 dense grid; Gabor jet: eight wavelengths and six orientations
EGM	0.029	±0.001	14 × 14 dense grid; Gabor jet: eight wavelengths and six orientations
GC-EGM	0.025	±0.001	14 × 14 dense grid; Gabor jet: eight wavelengths and six orientations
EGM	0.080	±0.003	11 vertices sparse grid; Gabor jet: four wavelengths and four orientations
GC-EGM	0.062	±0.002	11 vertices sparse grid; Gabor jet: four wavelengths and four orientations

the regions-of-interest would be notoriously different from the frontal-gaze case. Hence, considering that some images have deviated gaze, we used a method described in [24] to determine the eye corners, and used these as reference for defining the ROIs, obtaining a much more reliable definition of ROIs (Fig. 7).

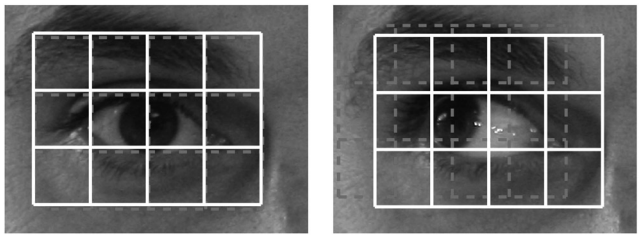

Fig. 7 *Comparison between the periocular regions-of-interest defined for a pair of images of the same subject, when using the method proposed by Park et al. [2] (dashed lines) and the geometric mean of eye corners as reference points (continuous lines)*

It is particularly important to perceive the effect of GC-EGM not only for different facial expressions, but also in cases where this factor is not evident. This is to prevent that GC-EGM might improve performance for different expressions, but has an opposite effect for similar expressions. Hence, the data set was divided into two subsets, as illustrated in Fig. 8: the first subset (set A) contains exclusively neutral facial expressions, and the second set (set B) includes seven facial expressions: neutral, angry, fear, disgust, happy, sad and surprise.

Results obtained for set A are shown in Fig. 9, where the left plot gives the density estimates of the genuine (light grey) and impostors (dark grey) matching scores, for the EGM (dashed lines) and GC-EGM (continuous lines) algorithms. The black lines give the genuine and impostors distributions when no compensation was carried out. The most obvious effect of the EGM/GC-EGM is in the genuine distribution, with a consistent movement away from the impostor scores. In this case, even though facial expressions are not evident, it is expected that 'micro-facial' expressions

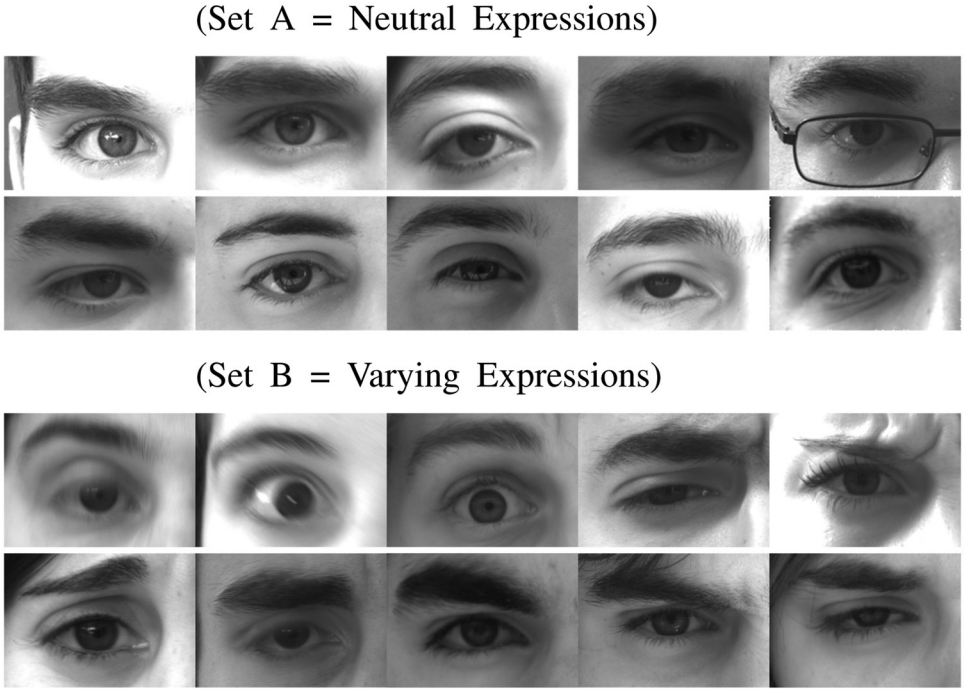

Fig. 8 *Examples of the data sets used in the evaluation of recognition performance*

In the upper set (A), all images have 'neutral' expression, whereas in the bottom set (B) images have varying facial expressions. Both sets contain significant variations in lighting conditions

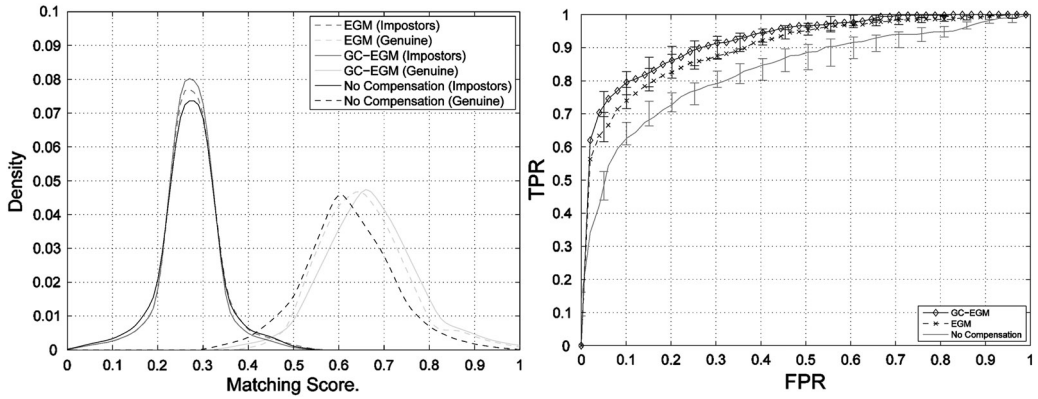

Fig. 9 *At left, comparison between the genuine/impostor distributions when using the EGM (dashed dark/light grey lines), GC-EGM (continuous dark/light grey lines) algorithms and when no compensation was carried out*

At right, the corresponding receiver operating characteristic curves. Results regarding data of neutral expression

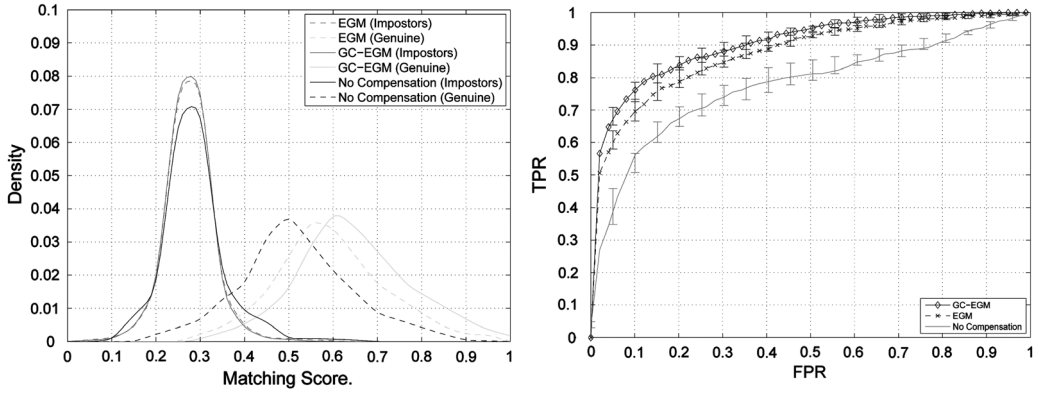

Fig. 10 *At left, comparison between the genuine/impostor distributions when using the EGM (dashed dark/light grey lines) and GC-EGM (continuous dark/light grey lines)*

At right, the corresponding receiver operating characteristic curves. Results regarding data of seven different facial expressions: neutral, angry, fear, disgust, happy, sad and surprise

remained and the effects of EGM/GC-EGM are still perceptible. Also, the impostors distribution remained invariant in the EGM/GC-EGM algorithms and in the 'no compensation' case. From the available pairwise comparisons, 90% of the genuine and 90% of the impostors were randomly drew and the recognition tests repeated 20 times, in order to obtain an estimate of the stability of the variations in performance. The right plot gives the corresponding receiver operating characteristic curves (ROCs) obtained, where the median performance at each point is represented by the line series and the horizontal bars denote the best/worst performance observed at each point.

The movement of the genuine distribution away from the impostors' is more evident in the results for 'set B' (Fig. 10). In this case, the distortions in the periocular region are far larger than in 'set A', justifying the improvements when using the EGM/GC-EGM algorithms. Comparing these algorithms, a more consistent increase of the genuine matching scores was observed for the GC-EGM, at a slightly inferior standard deviation. This suggests that results when using GC-EGM do not vary as much as in EGM, which was also observed for the impostors distribution (note the maximum density value of the GC-EGM genuine/impostor distributions in the left plot of Fig. 10). Also, the differences in performance between the EGM and GC-EGM are particularly evident in the ROC curves given at the right, where the confidence intervals for both algorithms do not intercept in the majority of the performance space.

5 Conclusions and further work

In the context of periocular recognition, this paper addressed the effectiveness of the EGM algorithm to compensate for distortions because of expressions. Having observed that the EGM is liable to changes in angular directions that are not biologically plausible, two modifications to that algorithm were proposed, aiming at: (i) improving the ability to handle local changes in rotation and (ii) reinforcing the topology preservation. A new term measures the similarity between jets and the edges cost term was reformulated, penalising changes in the orientation and reinforcing the preservation of the model topology.

Our experiments enabled us to observe decreases in the average registration errors between keypoints. Then, using the state-of-the-art periocular biometrics method, the recognition performance when using no compensation, using the EGM and the GC-EGM was assessed. Two main conclusions were drew: (i) algorithms to compensate for the effect of expressions consistently increase the recognition effectiveness, by moving the genuine distribution away

doi: 10.1049/iet-bmt.2013.0039

from the impostor scores and (ii) the proposed GC-EGM algorithm more faithfully handles the deformations inside the periocular region than the EGM. As a result, consistent increases in the recognition performance were observed when using the former algorithm. Finally, it should be stressed that such improvements were obtained without a substantial increase in the computational burden of the recognition process.

6 References

1 Daugman, J.G.: 'Probing the uniqueness and randomness of IrisCodes: results from 200 billion iris pair comparisons', *Proc. IEEE*, 2006, **94**, (11), pp. 1927–1935
2 Park, U., Jillela, R., Ross, A., Jain, A.K.: 'Periocular biometrics in the visible spectrum', *IEEE Trans. Inf. Forensics Sec.*, 2011, **6**, (1), pp. 96–106
3 Woodard, D., Pundlik, S., Miller, P., Jillela, R., Ross, A.: 'On the fusion of periocular and iris biometrics in non-ideal imagery'. Proc. 20th Int. Conf. Pattern Recognition (ICPR), 2010, pp. 201–204
4 Lades, M., Vorbruggen, J.C., Buhmann, J., *et al*.: 'Distortion invariant object recognition in the dynamic link architecture', *IEEE Trans. Comput.*, 1993, **42**, (3), pp. 300–311
5 Cao, Y., Zheng, W., Zhao, L., Zhou, C.: 'Expression recognition using elastic graph matching', *Lect. Notes Comput. Sci.*, 2005, **3784**, pp. 8–15
6 Zhao, S., Gao, W., Shan, S., Yin, B.: 'Enhance the alignment accuracy of active shape models using elastic graph matching'. Proc. First Int. Conf. Biometric Authentication, 2004, pp. 52–58
7 Stamou, G., Nikolaidis, N., Pitas, I.: 'Object tracking based on morphological elastic graph matching'. Proc. Int. Conf. Image Processing, 2005, vol. 1, pp. 709–712
8 Gosling, J.A., Harris, P.F., Humpherson, J.R., Whitmore, I., Willan, P.: 'Human anatomy: color atlas and textbook', ed. Bentley, A.L. (Mosby Elsevier, Philadelphia, 2008, 5th edn.)
9 Tefas, A., Kotropoulos, C., Pitas, I.: 'Using support vector machines to enhance the performance of elastic graph matching for frontal face authentication', *IEEE Trans. Pattern Anal. Mach. Intell.*, 2001, **23**, (7), pp. 735–746
10 Shin, H.-C., Park, J., Kim, S.-D.: 'Combination of warping robust elastic graph matching and kernel-based projection discriminant analysis for face recognition', *IEEE Trans. Multimed.*, 2007, **9**, (6), pp. 1125–1136
11 Zafeiriou, S., Tefas, A., Pitas, I.: 'Exploiting discriminant information in elastic graph matching'. Proc. Int. Conf. Image Processing (ICIP2005), 2005, vol. 3, pp. 768–771
12 Zafeiriou, S., Tefas, A., Pitas, I.: 'The discriminant elastic graph matching algorithm applied to frontal face verification', *Pattern Recognit.*, 2007, **40**, pp. 2798–2810
13 Zafeiriou, S., Pitas, I.: 'Discriminant graph structures for facial expression recognition', *IEEE Trans. Multimed.*, 2008, **10**, (8), pp. 1528–1540
14 Kela, N., Rattani, A., Gupta, P.: 'Illumination invariant elastic bunch graph matching for efficient face recognition'. Proc. Computer Vision and Pattern Recognition Workshop (CVPRW06), 2006, pp. 42
15 Shin, H., Kim, S.-D., Choi, H.-C.: 'Generalized elastic graph matching for face recognition', *Pattern Recognit. Lett.*, 2007, **28**, pp. 1077–1082
16 Kotropoulos, C., Tefas, A., Pitas, I.: 'Morphological elastic graph matching applied to frontal face authentication under well-controlled and real conditions', *Pattern Recognit.*, 2000, **33**, pp. 1935–1947
17 Serradell, E., Kybic, J., Noguer, F.M., Fua, P.: 'Robust elastic 2D/3D geometric graph matching', *Proc. SPIE Med. Imaging*, 2012, **8314**, pp. 831408
18 Daugman, J.G.: 'Complete discrete 2D gabor transform by neural networks for image analysis and compression', *IEEE Trans. Acoust. Speech Signal Process.*, 1988, **36**, (1), pp. 169–179
19 Wiskott, L., Fellous, J.-M., Krüger, N., vd Malsburg, C.: 'Face recognition by elastic bunch graph matching', *IEEE Trans. Pattern Anal. Mach. Intell.*, 1997, **19**, (7), pp. 775–779
20 Ojala, T., Pietikainen, M., Harwood, D.: 'A comparative study of texture measures with classification based on feature distributions', *Pattern Recognit.*, 1996, **29**, pp. 51–59
21 Dalal, N., Triggs, B.: 'Histograms of oriented gradients for human detection'. Proc. 2005 IEEE Computer Society Conf. Computer Vision and Pattern Recognition (CVPR05), 2005, vol. 1, pp. 886–893
22 Lowe, D.: 'Distinctive image features from scale-invariant keypoints', *Int. J. Comput. Vis.*, 2004, **60**, (2), pp. 91–110
23 Ross, A., Nandakumar, K., Jain, A.K.: 'Handbook of multibiometrics' (Springer-Verlag, New York, 2006)
24 Santos, G., Proença, H.: 'A robust eye-corner detection method for real-world data'. Proc. IEEE Int. Joint Conf. Biometrics, 2011, pp. 1–6